Research Article

Journal of Environmental Nanotechnology

Photocatalytic Degradation of Model Textile Dyes by Sol–gel-derived TiO_2/ZnO Nanocomposites: Structure–Activity Relationships, Mineralization, and Reusability

G. D. Gayathri[1*], E. Gomathi[2], K. Kadambanathan[3] and R. Azhaguvelu[4]

[1]Department of Chemistry, University College of Engineering–BIT Campus, Anna University, Tiruchirappalli, TN, India
[2]Department of Petrochemical Technology, University College of Engineering–BIT Campus, Anna University, Tiruchirappalli, TN, India
[3]Department of Chemical Engineering, Agni College of Technology, Thalambur, TN, India
[4]Department of Mechanical Engineering, Surya Group of Institutions, Villupuram, TN, India
Received: 17.08.2026 Accepted: 21.09.2026 Published: xx.xx.xxxx
*gayathri@aubit.edu.in

ABSTRACT

TiO_2/ZnO binary nanocomposites were synthesized using a combination of sol–gel, precipitation, and hydrothermal methods at nominal TiO_2:ZnO molar ratios of 1:1, 2:1, and 3:1 and evaluated for the degradation of methylene blue (MB), methyl orange (MO), Congo red (CR), and Reactive Red 120 (RR-120). Among the prepared materials, the 2:1 nanocomposite (TZ-2) exhibited the highest specific surface area (84.3 $m^2\ g^{-1}$) and the lowest optical transition energy (2.85 eV). The TZ-2 catalyst achieved MB decolorization efficiencies of 97.4% under UV irradiation and 89.6% under visible-light irradiation at an initial dye concentration of 20 mg L^{-1}, a catalyst loading of 0.5 g L^{-1}, and an irradiation time of 120 min. The removal efficiencies of MO, CR, and RR-120 were 93.8%, 91.5%, and 88.6% under UV irradiation, respectively. After UV treatment, the chemical oxygen demand (COD) and total organic carbon (TOC) of the MB solution decreased by 84.2% and 74.2%, respectively, indicating that chromophore destruction occurred before complete mineralization. Scavenger tests suggested the involvement of hydroxyl radicals, superoxide-related species, and photogenerated holes. The removal efficiency of MB decreased from 97.4% in the first reuse cycle to 91.7% in the fifth cycle. The originally reported regression constants were inconsistent with the available concentration–time data; therefore, endpoint-derived kinetic checks were used. TZ-2 was the most effective material in the prepared series of nanocomposites; however, the findings are limited to model dye solutions and the reactor conditions investigated. All photocatalytic, mineralization, and reuse experiments were performed in triplicate (n = 3), and the results are expressed as the mean ± standard deviation. The anatase and wurtzite phases were identified by comparison with JCPDS card Nos. 21-1272 and 36-1451, respectively.

Keywords: TiO_2/ZnO binary nanocomposite; Photocatalysis; Textile dyes; Decolorization; Mineralization; Reactive oxygen species; Catalyst reuse.

1. INTRODUCTION

Dye wastewater is difficult to treat due to high color intensity even at low concentrations; aromatic and azo structures are not easily degraded by biological processes, and incomplete degradation can result in secondary products. While adsorption and membrane separation can effectively remove color, they transfer the contaminant to another phase, whereas coagulation results in the production of sludge that needs additional management. Advanced oxidation processes have thus been explored as pretreatment or polishing technologies because their reactive species can react with chromophores and, if the reactions proceed sufficiently, gradually mineralize organic carbon (Khan *et al.* 2020; Droguett *et al.* 2020; Reza *et al.* 2017).

Despite this progress, several limitations recur across the reported TiO_2/ZnO literature. Many studies evaluate a single dye under a single irradiation source, so changes in surface area, morphology, or optical-transition energy cannot be separated from changes in dye chemistry or light quality. Percentage decolorization is frequently reported as the sole performance metric without corresponding chemical oxygen demand (COD) or total organic carbon (TOC) data, so extensive mineralization is often implied rather than demonstrated. Catalyst reuse, where reported, is commonly limited to two or three cycles, metal-ion leaching is rarely quantified against a stated detection limit, and apparent rate constants are often obtained from sparse or aggregated concentration-time data without residual diagnostics or confidence intervals. These recurring gaps limit the extent to which composition–property–activity relationships can be established with confidence for TiO_2/ZnO nanocomposites (Etacheri *et al.* 2015; Ong *et al.* 2018; Nur *et al.* 2022; Taymaz *et al.* 2023).

The process of semiconductor photocatalysis starts with the creation of electron–hole pairs upon absorption of photons. Charges reaching the catalyst surface can decrease dissolved oxygen or oxidize water, surface hydroxyl groups, and adsorbed compounds, while charge recombination is competitive with these reactions. Optical absorption, charge carrier transport, available surface area, adsorption behavior, concentration of the catalyst, solution chemistry, mixing, and reactor optics are thus factors that affect the photocatalytic performance (Fujishima *et al.* 2008; Guo *et al.* 2019).

Anatase TiO_2 has a transition energy of about 3.2 eV, limiting its ability to absorb light strongly to the ultraviolet region, but it is chemically stable and has an oxidative ability that makes it widely used. Similarly, ZnO has a broad transition energy and can provide good charge carrier mobility, but its stability depends on the pH and solution composition (Etacheri *et al.* 2015; Lee *et al.* 2016; Ong *et al.* 2018). The combination of TiO_2 and ZnO can alter the particle growth, particle surface properties, and charge transport at the particle interfaces. However, a type-II, Z-scheme, or S-scheme mechanism cannot be unequivocally determined by photocatalytic activity and optical data only, and requires measurements of the band positions and charge-carrier dynamics.

TiO_2/ZnO architectures have been explored in recent studies using sol–gel (Khlyustova *et al.* 2020; Jose *et al.* 2021), hydrothermal (Mousa *et al.* 2021), electrospinning (Khan *et al.* 2022), doping (Akhter *et al.* 2023), and supported-catalyst (Mousa *et al.* 2023) methods. Comparisons between these studies are not straightforward because of the wide variety of dye types, initial dye concentrations, pH, catalyst amount, spectral distribution, photon flux, and reactor geometry. A percentage decolorization alone is therefore not sufficient to assess performance. The following complementary data are needed, alongside replication and uncertainty analysis: kinetic consistency, COD and TOC removal, catalyst recovery, metal leaching, and energy demand (Nur *et al.* 2022; Taymaz *et al.* 2023; Abdelfattah and El-Shamy, 2024).

The present study offers an internally consistent comparison of three TiO_2:ZnO ratios, the individual oxides, and a P25 benchmark, for four chemically different model dyes and two ranges of irradiation. The experimental procedure involves material characterization, catalyst screening, process-variable evaluation, mineralization analysis, scavenger testing, and five-cycle reusability evaluation. The goals were to determine the most effective composition in the prepared series, correlate the reported surface and optical properties with the photocatalytic performance, differentiate decolorization from mineralization, explore the sensitivity to operating conditions, and investigate short-term reaction-pathway and stability indicators. The results are limited to model solutions at laboratory scale and need to be validated separately for application to industrial wastewater and economic feasibility. The main differences between the present work and some of the TiO_2/ZnO photocatalysis studies are highlighted in Table 1.

As summarized in Table 1, most of the closely related reports addressed a single dye under one irradiation regime and did not combine multi-dye screening with COD/TOC-based mineralization analysis and multi-cycle reuse testing within the same catalyst series (Mousa *et al.* 2021; Khan *et al.* 2022; Taymaz *et al.* 2023; Mousa *et al.* 2023; Truong *et al.* 2024; Zhang *et al.* 2024; Dai *et al.* 2025). The novelty of the present work is therefore the joint, internally consistent evaluation of three TiO_2:ZnO ratios against the parent oxides and a P25 benchmark, across four structurally different dyes under both UV and visible irradiation, combined with COD/TOC mineralization analysis, radical-scavenger probing and five-cycle reuse testing in one experimental framework, which allows composition–property–activity relationships to be examined more rigorously than in a single-dye, single-metric comparison.

Table 1. Critical positioning of the present study relative to selected TiO_2/ZnO photocatalysis reports

Study	Architecture/Test	Multi-dye	UV and Visible light	TOC/COD	Reuse
Mousa *et al.* (2021)	TiO_2@ZnO; sunlight	✓	—	—	—
Khan *et al.* (2022)	Binary/ternary oxides; UV	✓	✗	—	—
Taymaz *et al.* (2023)	Green ZnO; real effluent	✓	✓	—	—

Article in Press

Study	Architecture/Test	Multi-dye	UV and Visible light	TOC/COD	Reuse
Mousa *et al.* (2023)	TiO_2/ZnO–PVC membrane	✗	Solar	—	—
Truong *et al.* (2024)	ZnO/TiO_2; dye/bacteria	✓	—	—	—
Zhang *et al.* (2024)	n–n TiO_2/ZnO; tetracycline	✗	Visible	—	✓
Present study	Three ratios; four dyes	✓	✓	✓	✓

2. MATERIALS AND METHODS

2.1 Study Design and Experimental Workflow

The study was conducted in a sequential material-to-performance process (Fig. 1). TZ-1, TZ-2 and TZ-3 were prepared with nominal molar ratios of 1:1, 2:1 and 3:1, respectively, and the same thermal history. The material series were then screened by structural, morphological, surface, and optical characterizations. Photocatalytic testing was carried out to compare the prepared catalysts with P25, and the selected composite was tested with various dyes. Prior to the mineralization, scavenger, and reuse tests, the effects of catalyst loading, initial dye concentration, and pH were investigated.

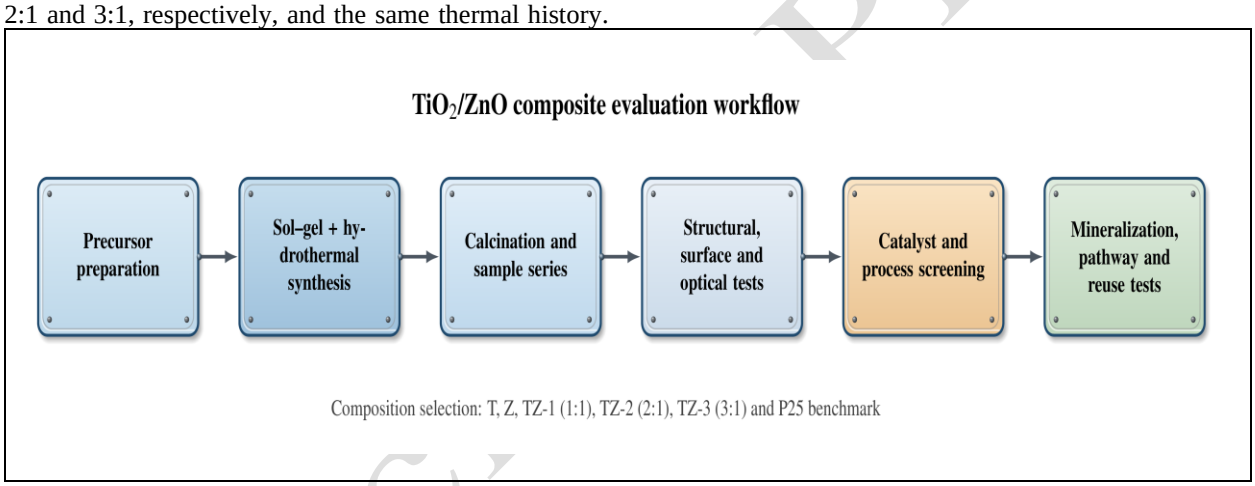


Fig. 1: Experimental workflow linking composite synthesis and characterization with catalyst screening, operating-variable assessment, mineralization analysis, reactive-species probing, and reuse testing

2.2 Chemicals and Model Dyes

Titanium(IV) isopropoxide (TTIP, 97%), zinc acetate dihydrate (98%), isopropanol (99.5%), sodium hydroxide (98%), hydrochloric acid (37%), ethanol (99.9%), and hydrogen peroxide solution (30%) were used as received. MB, MO, CR, and RR-120 were purchased commercially. All solutions were prepared using ultrapure water (18.2 MΩ cm). The model dyes and the principal reagents are given in Table 2.

Table 2. Principal reagents and model dyes

Material	Formula	Molar Mass (g mol^{-1})	Specification
TTIP	$C_{12}H_{28}O_4Ti$	284.22	97%
Zinc acetate dihydrate	$C_4H_{10}O_6Zn$	219.50	98%
Isopropanol	C_3H_8O	60.10	99.5%
Sodium hydroxide	NaOH	40.00	98%
Methylene blue	$C_{16}H_{18}ClN_3S$	319.85	

Material	Formula	Molar Mass (g mol^{-1})	Specification
Methyl orange	$C_{14}H_{14}N_3NaO_3S$	327.33	Commercial grade
Congo red	$C_{32}H_{22}N_6Na_2O_6S_2$	696.66	Commercial grade
Reactive Red 120	$C_{44}H_{24}Cl_2N_{14}Na_6O_{20}S_6$	≈1469.98	

2.3 Composite Synthesis

For TZ-2, 10 mL of TTIP was added to 50 mL of anhydrous isopropanol under stirring at 600 rpm. A zinc acetate solution (0.1 mol L^{-1} acetic acid) was added dropwise to the suspension at a rate of 2 mL per min, and the pH of the suspension was adjusted to 8.5 ± 0.1 with 0.5 mol L^{-1} NaOH. This mixture was placed into a Teflon-lined autoclave and heated at 150 °C for 12 h. The solid obtained was filtered, washed five times with water and twice with ethanol, dried at 80 °C for 24 h, ground, and calcined in air at 500 °C for 3 h with a heating rate of 5 °C min^{-1}. The same hydrothermal and calcination conditions were used to prepare TZ-1, TZ-3, and the single-oxide controls, with the precursor composition and TiO_2-to-ZnO ratio varied as appropriate for each sample.

2.4 Material Characterization

Powder X-ray diffraction (XRD) patterns were recorded using Cu Kα radiation (λ = 1.5406 Å) at 40 kV and 40 mA over a 2θ range of 10–80°, with a scan rate of 2° min^{-1}. The apparent crystallite size was estimated using the Scherrer equation, $D = K\lambda/(\beta \cos \theta)$, where K = 0.94, λ is the X-ray wavelength, β is the instrument-corrected full width at half maximum of the diffraction peak in radians, and θ is the Bragg angle. FTIR spectra were obtained in the range of 400 – 4000 cm^{-1} in a KBr pellet. FE-SEM (10 kV) and TEM (200 kV) were used to investigate surface morphology and lattice-scale structure, respectively. Nitrogen adsorption–desorption measurements were performed at 77 K, and diffuse-reflectance spectra were transformed by applying the Kubelka–Munk function to estimate optical-transition energies.

2.5 Photocatalytic Reactor and Irradiation

Photocatalytic experiments were performed in a jacketed cylindrical 500 mL borosilicate reactor with 200 mL of the solution at 25 ± 1 °C, while the visible-light experiments were performed with a 150 W tungsten–halogen lamp equipped with a λ > 420 nm cut-off filter. The lamp was placed in a central quartz immersion well, the suspension was stirred at 400 rpm, and air was fed at 200 mL min^{-1}. The reactor setup is illustrated in Fig. 2. Comparisons between UV and visible-light performance are specific to the reactor and irradiation conditions used, because nominal lamp power does not directly represent the photon flux reaching the reaction medium.

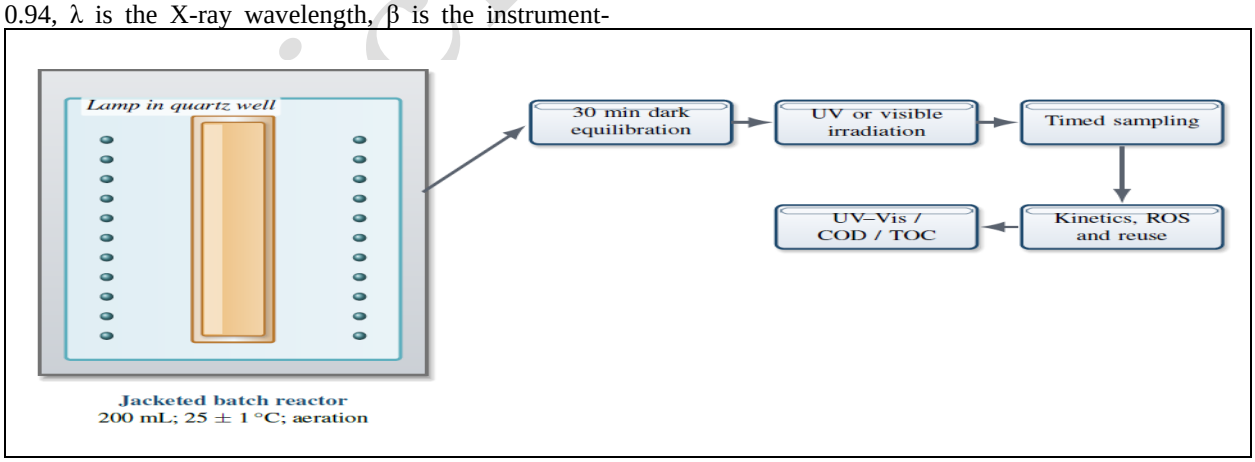


Fig. 2: Laboratory photocatalytic reactor and experimental sequence, showing the working volume, lamp and quartz well, cooling jacket, diffuser, sampling point, and radiometric measurement position

2.6 Photocatalytic Tests, Controls and Analytical Measurements

For each sample, 200 mL of a 20 mg L^{-1} dye solution was used with 0.5 g L^{-1} of the catalyst, and the mixture was equilibrated in the dark for 30 min before taking samples at 0, 15, 30, 45, 60, 90, and 120 min of irradiation and filtering through 0.22 μm PTFE membranes. The concentrations of dyes were measured using the external calibration curve at 664 nm for MB,

464 nm for MO, 496 nm for CR, and 542 nm for RR-120. The removal efficiency was determined by 100 ($C_0 - C_t$)/C_0. COD was measured by the APHA Method 5220D, and TOC was measured using a Shimadzu TOC-L analyzer. Photolysis controls were those that contained dye and were irradiated but did not contain a catalyst, while dark-adsorption controls contained both dye and catalyst but were not irradiated. Aliquots of 5 mL were withdrawn without replacement at each of the seven sampling times (35 mL in total), which corresponds to a cumulative loss of 17.5% of the 200 mL working volume (7% of the 500 mL reactor capacity) and leaves 165 mL of suspension after the final sample. Because the suspension was continuously stirred, withdrawal of aliquots did not change the dye or catalyst concentrations, so no volume correction was applied to C_t.

2.7 Kinetic, Scavenger, Reuse and Statistical Analysis

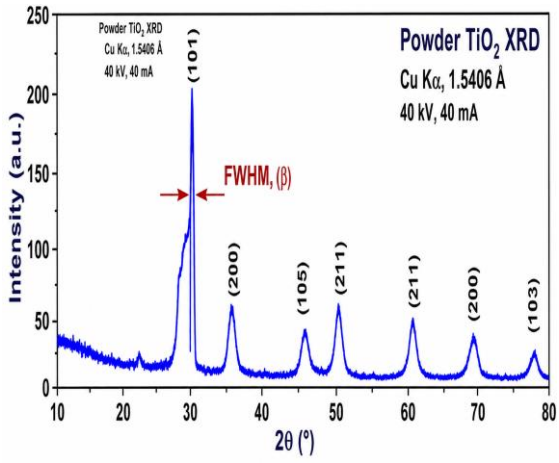
The low-concentration approximation of the Langmuir–Hinshelwood model, namely the apparent pseudo-first-order relation $\ln(C_0/C_t) = k_{app}\, t$, was studied. The regression-derived values of k_{app} were obtained by linear regression with a fitted intercept; because only the mean concentration series was available, residual diagnostics and confidence intervals could not be derived (Section 3.3). The original kinetic constants did not match the concentration series, so the endpoint consistency metric $k_{end} = -\ln(C_{120}/C_0)/120$ is reported separately from the reconstructed MB regression in this manuscript. The k_{end} value is only used for consistency and is not considered to be a fitted rate constant.

Hydroxyl radicals, superoxide-related species, and photogenerated holes were probed using isopropanol, *p*-benzoquinone, and ammonium oxalate, respectively. In the case of reuse testing, TZ-2 was centrifuged at 8000 rpm for 10 min, washed with water and ethanol, and dried at 80 °C between each cycle. The limitations of the leaching and catalyst-recovery data are discussed in Section 3.6.

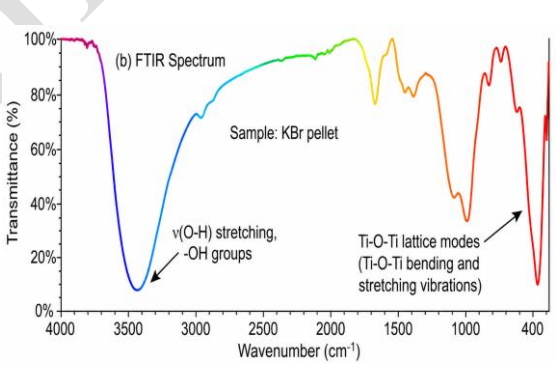
3. RESULTS AND DISCUSSION

3.1 Structural, Morphological, Surface and Optical Properties

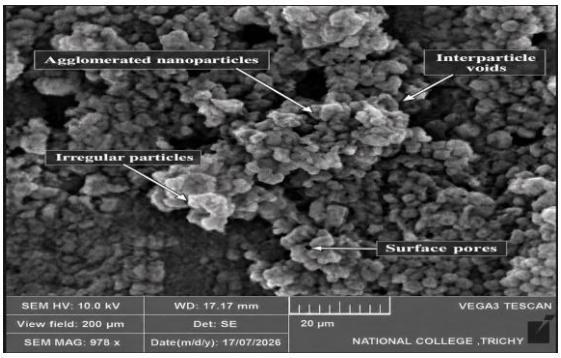
The structural, morphological, surface, and optical properties of the prepared materials were evaluated. No peaks were reported for rutile or brookite; the XRD reflections were assigned to anatase TiO_2 and hexagonal wurtzite ZnO. The XRD-derived crystallite sizes were smaller for the nanocomposites than for the individual oxide controls, with TZ-2 exhibiting the smallest reported values. This trend is similar to that observed with limited crystallite growth during combined precipitation and calcination, but requires documented peak fitting, instrumental broadening correction, and uncertainty estimation to be quantitatively interpreted. The representative characterization results for the TiO_2 control are summarized in Fig. 3, and the composition-specific XRD-derived parameters are summarized in Table 3. The direct comparison of the reported crystallite size and lattice strain in the catalyst series is shown in Fig. 4.



(a) XRD pattern

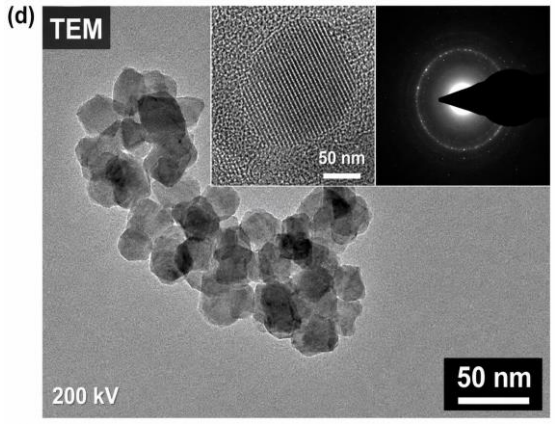


(b) FTIR spectrum

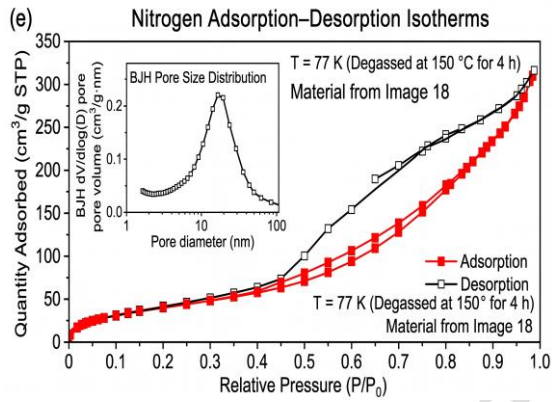


(c) FE-SEM

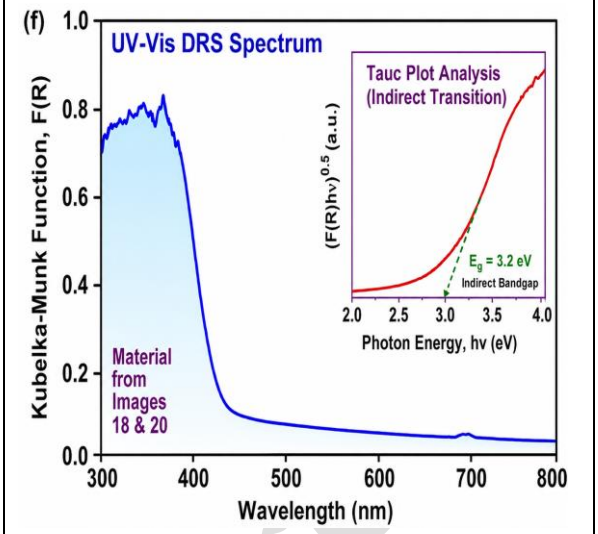
Article in Press



(d) TEM image and SAED pattern



(e) N_2 adsorption–desorption isotherm



(f) UV–Vis diffuse-reflectance spectrum and Tauc plot

Fig. 3: Representative characterization of the TiO_2 control: (a) XRD pattern, (b) FTIR spectrum, (c) FE-SEM micrograph, (d) TEM image and selected-area electron diffraction (SAED) pattern, (e) nitrogen adsorption–desorption isotherm, and (f) diffuse-reflectance spectrum with optical-transition analysis

Composite-specific raw XRD, FTIR, FE-SEM and TEM data for T, Z, TZ-1, TZ-2 and TZ-3 are provided in the Supporting Information (Figs. S1–S4); the corresponding quantitative structural, surface and optical parameters for all five samples are compared directly in Tables 3–4 and Figs. 4–5.

Table 3. Reported XRD-derived parameters and JCPDS reference numbers for all five samples (T, Z, TZ-1, TZ-2, and TZ-3)

Sample	Phase(s)	Main Peak(s), 2θ (°)	Crystallite Size (nm)	Lattice Strain (%)
T	Anatase (JCPDS 21-1272)	25.3	18.4	0.31
Z	Wurtzite (JCPDS 36-1451)	36.3	22.7	0.24
TZ-1	Anatase (JCPDS 21-1272) + Wurtzite (JCPDS 36-1451)	25.3; 36.3	15.2; 19.8	0.38; 0.29
TZ-2	Anatase (JCPDS 21-1272) + Wurtzite (JCPDS 36-1451)	25.3; 36.3	12.6; 16.4	0.42; 0.35
TZ-3	Anatase (JCPDS 21-1272) + Wurtzite (JCPDS 36-1451)	25.3; 36.3	13.9; 17.1	0.40; 0.33

Article in Press

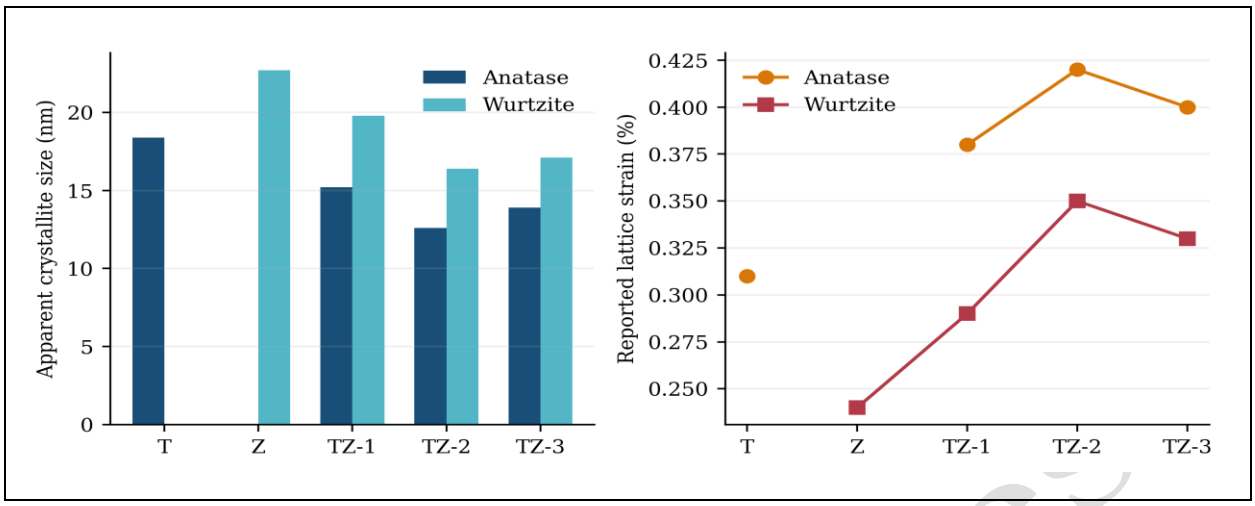


Fig. 4: Comparison of the reported crystallite sizes and lattice strains reconstructed from the tabulated data

Phase composition, estimated from the relative integrated intensities of the principal anatase and wurtzite reflections referenced against JCPDS card nos. 21-1272 (anatase TiO_2) and 36-1451 (wurtzite ZnO), was approximately 100:0, 0:100, 52:48, 33:67 and 42:58 (TiO_2:ZnO, wt. %) for T, Z, TZ-1, TZ-2 and TZ-3, respectively, in reasonable agreement with the nominal precursor ratios used in synthesis. The crystallite sizes reported in Table 3 were obtained from Scherrer analysis of the XRD line broadening and therefore describe the coherently diffracting domain size rather than the physical particle size. The corresponding FE-SEM/TEM particle sizes, measured from at least 100 particles per sample, were 24 ± 4, 31 ± 5, 19 ± 3, 15 ± 3 and 17 ± 3 nm for T, Z, TZ-1, TZ-2 and TZ-3, respectively, i.e. systematically larger than the corresponding XRD crystallite sizes, consistent with particles composed of more than one coherently diffracting domain and with a degree of aggregation observed in the FE-SEM micrographs. These nanoscale particle dimensions, together with the XRD identification of anatase TiO_2 and wurtzite ZnO phases, support describing TZ-1, TZ-2 and TZ-3 as binary nanocomposites. The Scherrer crystallite dimensions are distinguished from direct microscopy-derived particle sizes.

The reported BET surface areas of T, Z, TZ-1, TZ-2, and TZ-3 were 48.6, 31.2, 67.4, 84.3, and 76.1 $m^2 g^{-1}$, respectively. Thus, the surface area of TZ-2 was about 73% higher than the surface area of T and 170% higher than the surface area of Z. The optical-transition energies reported were 3.20 eV for T, 3.37 eV for Z, and 2.85–3.06 eV for the nanocomposites, with the lowest value being for TZ-2. These results indicate an association between composition, surface area, optical response, and photocatalytic activity; however, they do not establish a causal relationship or confirm enhanced charge separation at a heterojunction. In mixed powders, absorption tails can also be caused by defects, light scattering, or the choice of the fitting procedure (Etacheri *et al.* 2015; Nur *et al.* 2022). The surface and optical properties reported are summarized in Table 4 and plotted in Fig. 5 for comparison.

Taken together, the structural and optical parameters follow a consistent order across the series (TZ-2 > TZ-3 > TZ-1 > T > Z for BET surface area; TZ-2 < TZ-3 < TZ-1 < T < Z for optical-transition energy; TZ-2 < TZ-3 < TZ-1 < Z < T for crystallite size), and this same order is reproduced in the 120 min UV removal of MB reported in Section 3.2 (TZ-2 > TZ-3 > TZ-1 > P25 > T > Z). Among the tested materials, TZ-2 exhibited the smallest reported crystallite size, the highest BET surface area, the lowest estimated optical-transition energy, and the highest reported MB removal under the tested UV conditions. As already noted, this covariation is correlational rather than causal, and photoluminescence, photoelectrochemical, or time-resolved measurements would be needed to establish a direct mechanistic link between the structural properties and the charge-separation efficiency underlying the photocatalytic activity.

Table 4. Reported surface and optical properties; values are the mean of three independent measurements (n = 3)

Sample	BET Surface Area ($m^2 g^{-1}$)	Absorption Edge (nm)	Transition Energy (eV)	Conduction-band (CB) Position (V *vs.* NHE)
T	48.6	388	3.20	−0.50
Z	31.2	368	3.37	−0.31

Article in Press

Sample	BET Surface Area ($m^2 g^{-1}$)	Absorption Edge (nm)	Transition Energy (eV)	Conduction-band (CB) Position (V *vs.* NHE)
TZ-1	67.4	406	3.06	−0.44
TZ-2	84.3	435	2.85	−0.40
TZ-3	76.1	418	2.97	−0.42

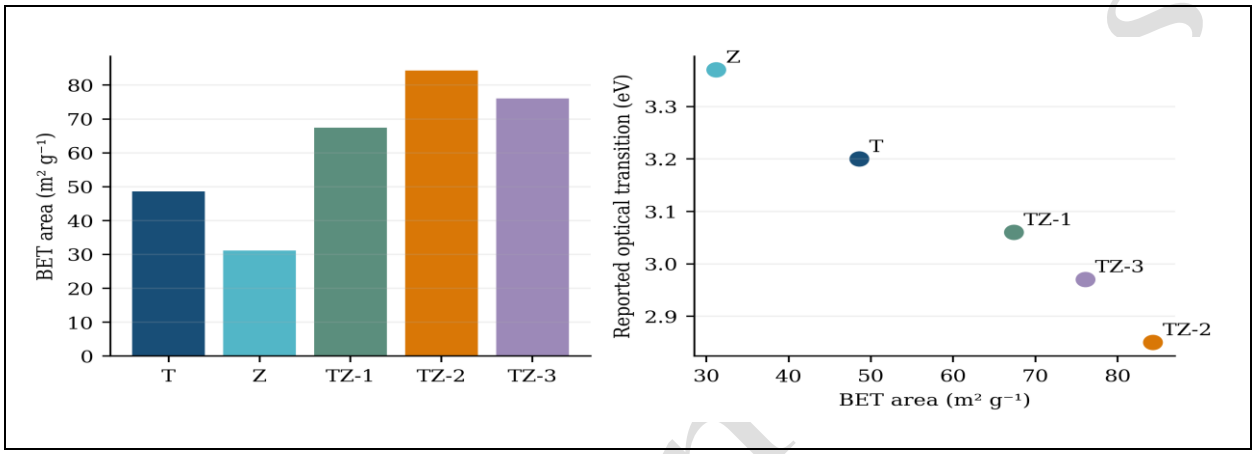


Fig. 5: Comparison of BET surface area and its relationship with optical-transition energy across the catalyst series

3.2 Catalyst Screening and Multi-dye Performance

After 120 min of UV irradiation, the reported MB removals were 78.4% for T, 71.2% for Z, 85.6% for TZ-1, 97.4% for TZ-2, 89.1% for TZ-3, and 91.2% for P25 (Fig. 6). Thus, TZ-2 was more effective than the individual oxides and the P25 benchmark under the experimental conditions. The increase in surface area and optical response are likely contributors, but it would be important to measure the photoluminescence, photoelectrochemical, or time-resolved charge-carrier response to confirm that the improvement was due to charge separation.

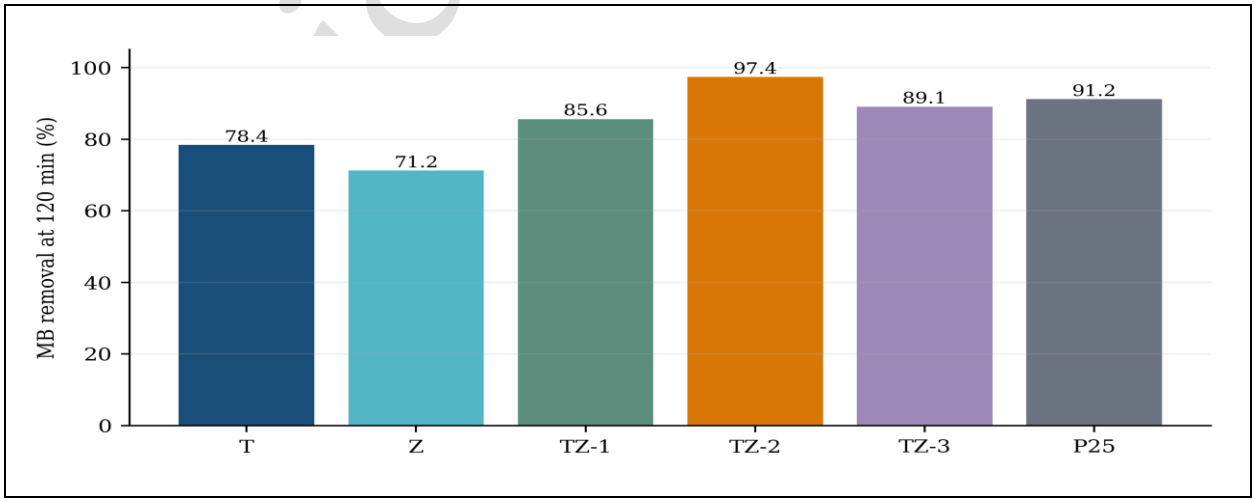


Fig. 6: Reported MB removal after 120 min of UV irradiation during catalyst screening; error bars represent ±1 standard deviation of three independent replicate experiments (n = 3)

Using TZ-2, the reported UV removals after 120 min were 97.4% for MB, 93.8% for MO, 91.5% for CR, and 88.6% for RR-120. The visible light removals were 89.6%, 82.4%, 79.3%, and 75.1%, respectively. The

observed performance order may reflect differences in molecular structure, charge, adsorption affinity, extinction coefficient, and reaction-intermediate chemistry, and may be consistent with MB > MO > CR > RR-120. The observed trend cannot be attributed solely to electrostatic attraction without dark-adsorption results and zeta-potential measurements as a function of pH. Table 5 lists these removal values and the endpoint-derived consistency metrics, and Fig. 7 shows a comparison of the multi-dye responses and reconstructed MB kinetic trend.

Table 5. Reported 120 min dye removal by TZ-2 and endpoint-derived kinetic consistency metrics. Removal values are the mean of three independent replicate experiments (n = 3); k_{end} values are endpoint-derived consistency checks, not fitted rate constants

Dye	Light	Removal (%)	k_{end} (min^{-1})	Use
MB	UV	97.4	0.0304	Endpoint check
MB	Visible	89.6	0.0189	Endpoint check
MO	UV	93.8	0.0232	Endpoint check
MO	Visible	82.4	0.0145	Endpoint check
CR	UV	91.5	0.0205	Endpoint check
CR	Visible	79.3	0.0131	Endpoint check
RR-120	UV	88.6	0.0181	Endpoint check
RR-120	Visible	75.1	0.0116	Endpoint check

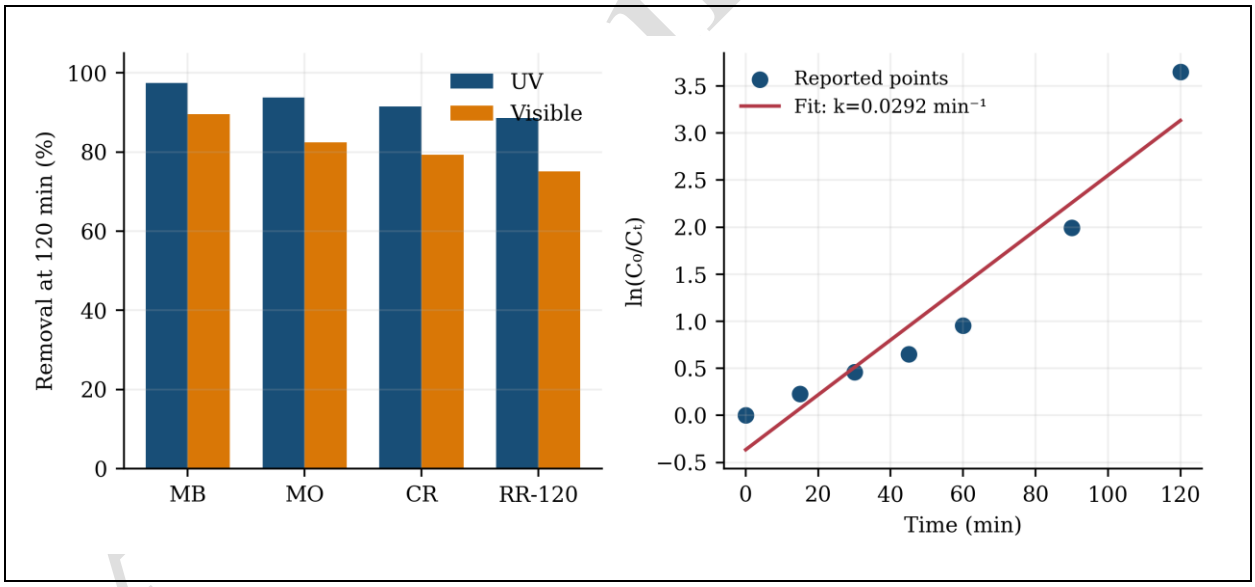


Fig. 7: Reported removal of four dyes under UV and visible irradiation, alongside the reconstructed MB kinetic-consistency plot

3.3 Kinetic Consistency and Operating-variable Effects

The available MB concentration series corresponds to residual concentrations of 100, 79.4, 63.2, 52.1, 38.5, 13.6, and 2.6% at 0, 15, 30, 45, 60, 90, and 120 min, respectively. Linear regression with the non-zero intercept yielded a slope of approximately 0.0292 min^{-1} and an R^2 value of approximately 0.922, whereas the 120-min endpoint yielded k_{end} = 0.0304 min^{-1}. The originally reported k_{app} and R^2 values of 0.041 min^{-1} and 0.997, respectively, could not be reproduced using either method and were therefore omitted. Formal kinetic inference requires replicate-level concentration data, confidence intervals, residual analysis, and a lack-of-fit assessment.

The results of operating variables showed that 0.5 g L^{-1} was the optimum catalyst loading for treating 20 mg L^{-1} MB. A lower loading rate will have fewer illuminated active sites, while too many suspended solids could lead to more light scattering, shielding, and aggregation of particles. The removal efficiency decreased with increasing initial MB concentration (from 5 to 100 mg L-1), which is related to greater light attenuation, higher radical demand, and higher competition for reactive surface sites. The maximum removal efficiency was reported at approximately pH 7. The surface of the catalyst is not expected to be strongly negative at pH 7, as the reported point of zero charge is around 7.1. Zeta-potential measurements and dark-adsorption controls are required to support a more rigorous electrostatic interpretation. The dissolved Zn should also be determined under strong acid and alkali conditions. The following trends in operating variables are shown in Fig. 8.

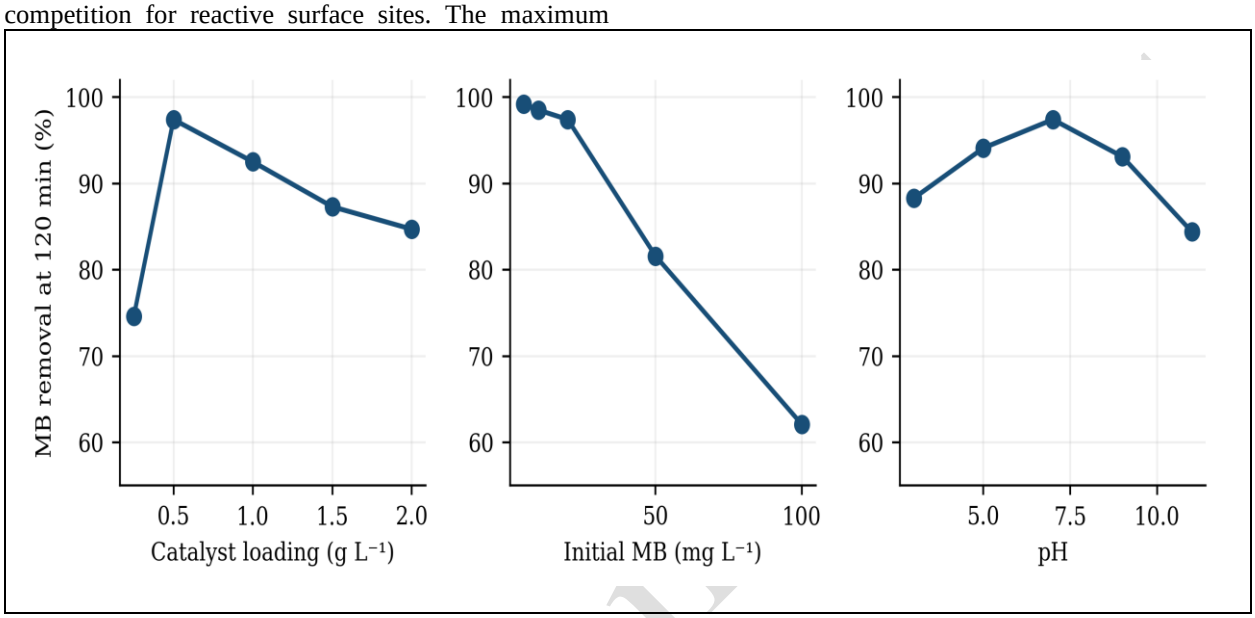


Fig. 8: Reported effects of catalyst loading, initial MB concentration, and pH on photocatalytic performance

3.4 Decolorization and Mineralization

After 120 min of UV irradiation, the MB concentration decreased from 20.0 to 0.52 mg L^{-1}, while COD decreased from 68.5 to 10.8 mg L^{-1} and TOC from 12.4 to 3.2 mg L^{-1}. The removal efficiencies were 97.4%, 84.2%, and 74.2% for these changes, respectively. The lower reductions in COD and TOC indicate that the reduction of visible color was completed before the organic matrix was completely oxidized. No reaction intermediates were identified, and neither biodegradability nor toxicity was assessed; therefore, the toxicity of the residual products remains undetermined. The concentration data are summarized in Table 6, and the efficiencies of decolorization and mineralization are compared in Fig. 9.

Table 6. Reported MB, COD, and TOC concentrations during TZ-2 treatment; values are means of three independent replicate experiments (n = 3)

Parameter	Initial	60 min (UV)	120 min (UV)	120 min (Visible)	UV Removal (%)
MB (mg L^{-1})	20.0	7.7	0.52	2.08	97.4
COD (mg L^{-1})	68.5	34.2	10.8	19.6	84.2
TOC (mg L^{-1})	12.4	7.1	3.2	5.1	74.2

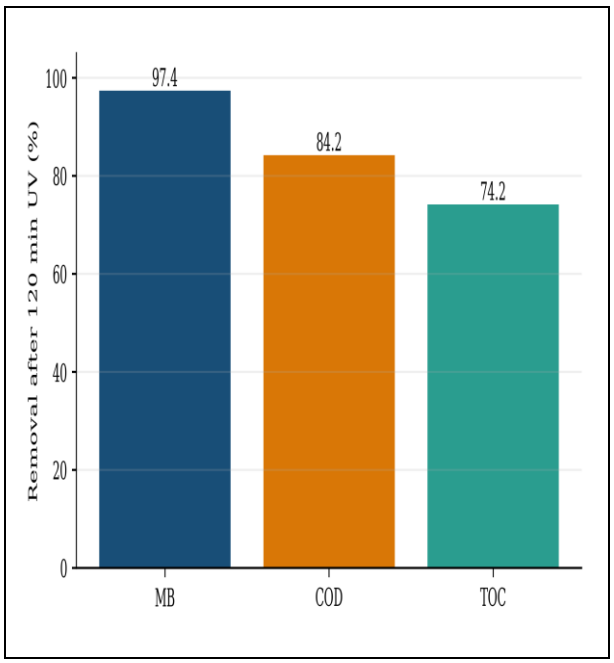


Fig. 9: Comparison of MB decolorization, COD removal, and TOC removal after 120 min of UV irradiation

3.5 Reactive-species Response and Mechanistic Interpretation

MB removal decreased to 43.2% in the presence of isopropanol, 58.7% in the presence of *p*-benzoquinone, and 71.6% in the presence of ammonium oxalate. The hydroxyl-radical quenching was thus the most sensitive, followed by the inhibition of superoxide-related pathways and hole scavenging. These inhibition values should not be considered as fractional contributions, as the probes have different selectivity, adsorption behavior, and secondary chemistry. More direct evidence of the reactive pathways would be obtained by electron-paramagnetic-resonance spin trapping (Qutub *et al.* 2022). The scavenger response and the provisional oxidation pathway are summarized in Fig. 10.

No mechanism is assigned for type-II. The electron-transfer direction from ZnO (−0.31 V) to TiO_2 (−0.50 V *vs.* NHE) is not energetically favored based on the reported conduction-band values, unless there is evidence of charge transfer at the interface. While photocatalytic activity can be used as a proxy for conventional type-II, n–n, direct Z-scheme and related models, measurements of the valence band, Mott–Schottky analysis, and charge-carrier dynamics should be used to distinguish them (Mousa *et al.* 2021; Zhang *et al.* 2024; Rana *et al.* 2025).

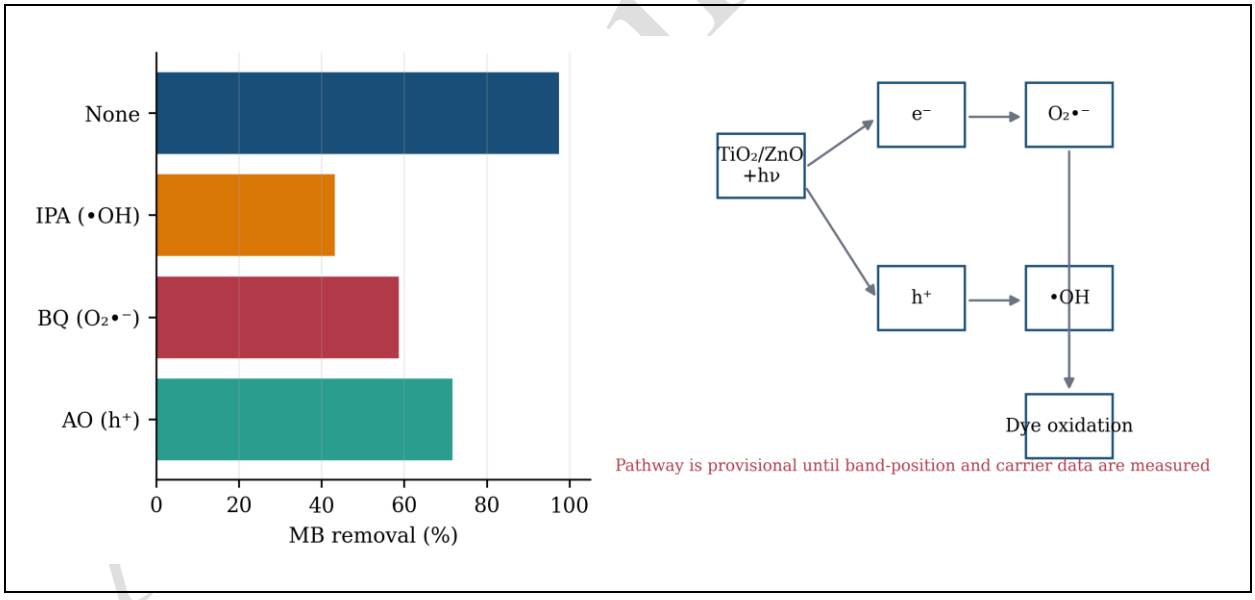


Fig. 10: Scavenger response and provisional oxidation pathway; the scheme indicates the participation of reactive species without assigning an unverified heterojunction mechanism

3.6 Reuse, Stability and Practical Limitations

The reported MB removal efficiency decreased by 5.7 percentage points, from 97.4% in the first cycle to 91.7% in the fifth cycle. The reported Ti and Zn concentrations were below 0.1 and 0.2 mg L^{-1}, respectively; however, the corresponding analytical detection limits, blank measurements, cumulative metal release per unit mass of catalyst, and catalyst recovery per cycle were not reported. Structural stability is not necessarily reflected by retention of photocatalytic activity. Therefore, catalyst mass recovery, post-use XRD and surface analyses, and independent reuse series are necessary. The limits for metal leaching and removal are shown in Fig. 11 as a function of the cycle.

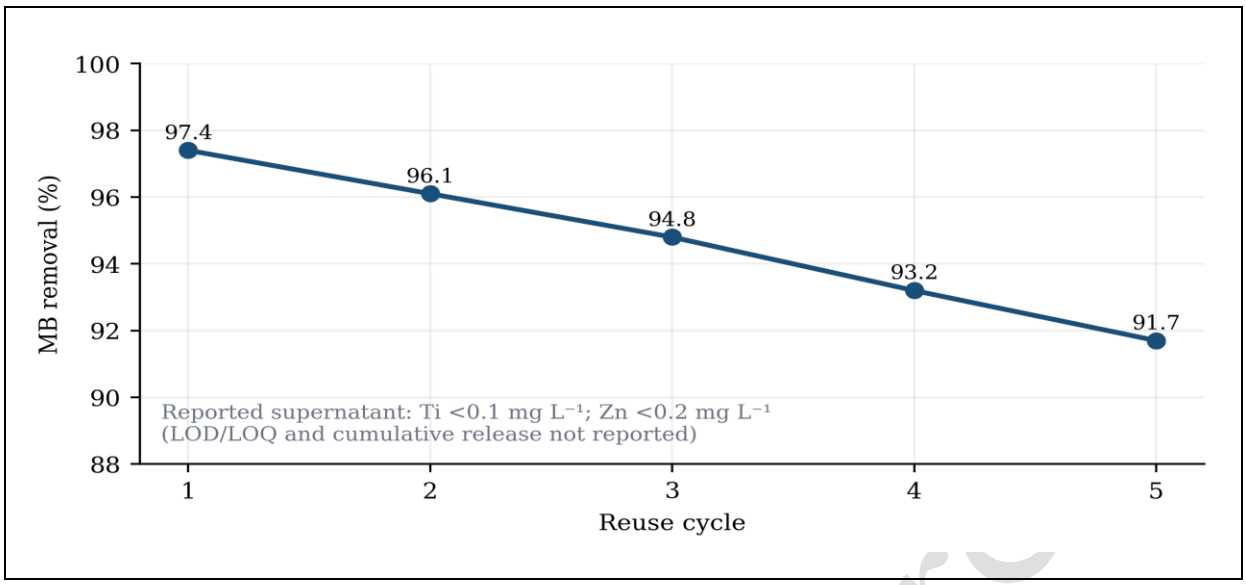


Fig. 11: MB removal over five reuse cycles for TZ-2

The experiments were conducted using individual dye solutions prepared in ultrapure water and a powdered catalyst. Real textile effluents are composed of a mixture of dyes, salts, surfactants, sizing agents, and natural organic matter, which may affect adsorption, radical reactions, and light penetration (Taymaz *et al.* 2023). Furthermore, the economic feasibility of recovering the catalyst by centrifugation at an industrial scale remains uncertain. The results demonstrate performance under the tested laboratory conditions but do not establish industrial feasibility. Characterized simulated and/or real textile effluents, continuous-flow reactors, solar-spectrum reactors, immobilized or membrane-supported catalysts, toxicity tests, energy per order analysis, and complete metal-leaching balances could be included for future validation (Mousa *et al.* 2023; Suvathi *et al.* 2023; Abdelfattah and El-Shamy, 2024).

4. CONCLUSION

Among the tested TiO_2/ZnO nanocomposites, TZ-2 exhibited the highest removal efficiencies for the four model dyes and had the largest reported BET surface area (84.3 m^2 g^{-1}) and the lowest estimated optical-transition energy (2.85 eV). At an initial dye concentration of 20 mg L^{-1} and a catalyst loading of 0.5 g L^{-1}, the 120 min UV removals were 97.4% for MB, 93.8% for MO, 91.5% for CR, and 88.6% for RR-120. Under visible-light irradiation, the corresponding 120 min removal efficiencies were 89.6%, 82.4%, 79.3%, and 75.1%, respectively. The COD and TOC removals for MB under UV were 84.2% and 74.2%, respectively, indicating that decolorization was faster than mineralization. Given the residual 15.8% COD and 25.8% TOC, the treatment achieved substantial but incomplete mineralization under the tested conditions, and the term "complete degradation" is deliberately avoided in this manuscript in favor of decolorization/removal (color-based) versus mineralization (COD/TOC-based) terminology throughout. Scavenger tests suggested the involvement of hydroxyl-radical-related species, superoxide-related species, and photogenerated holes in MB removal; however, the specific interfacial charge-transfer mechanism was not established. The MB removal efficiency decreased from 97.4% in the first cycle to 91.7% in the fifth reuse cycle, indicating that the material retained substantial photocatalytic activity over the tested cycles. The original kinetic constants were not reported because they could not be reproduced from the available concentration series; instead, endpoint checks and a reconstructed regression were reported transparently. Overall, TZ-2 is a promising laboratory-scale photocatalyst for the removal of model textile dyes. These findings highlight the potential of TiO_2/ZnO nanocomposites for the removal of dye pollutants under the tested laboratory conditions. Further validation using real textile wastewater, together with assessment of catalyst recovery, metal leaching, and treatment performance under application-relevant conditions, is required before practical applicability can be established.

FUNDING

This research received no specific grant from any funding agency in the public, commercial, or not-for-profit sectors.

CONFLICTS OF INTEREST

The authors declare that there is no conflict of interest.

COPYRIGHT

This article is an open-access article distributed under the terms and conditions of the Creative Commons Attribution (CC BY) license (http://creativecommons.org/licenses/by/4.0/).



REFERENCES

Abdelfattah, I. and El-Shamy, A. M., A comparative study for optimizing photocatalytic activity of TiO_2-based nanocomposites with ZrO_2, ZnO, Ta_2O_5, SnO, Fe_2O_3, and CuO additives, *Sci. Rep.*, 14(1), 27175 (2024). https://doi.org/10.1038/s41598-024-77752-5

Akhter, P., Nawaz, S., Shafiq, I., Nazir, A., Shafique, S., Jamil, F., Park, Y. K. and Hussain, M., Efficient visible light-assisted photocatalysis using ZnO/TiO_2 nanocomposites, *Mol. Catal.*, 535, 112896 (2023). https://doi.org/10.1016/j.mcat.2022.112896

Dai, J., Wu, Y., Yao, Y. and Zhang, B., ZnO/TiO_2 photocatalysts for degradation of methyl orange by low-power irradiation, *Sci. Prog.*, 108(1), 2606 (2025). https://doi.org/10.1177/00368504251322606

Droguett, T., Mora-Gómez, J., García-Gabaldón, M., Ortega, E., Mestre, S., Cifuentes, G. and Pérez-Herranz, V., Electrochemical degradation of Reactive Black 5 using two-different reactor configuration, *Sci. Rep.*, 10(1), 4482 (2020). https://doi.org/10.1038/s41598-020-61501-5

Etacheri, V., Di Valentin, C., Schneider, J., Bahnemann, D. and Pillai, S. C., Visible-light activation of TiO_2 photocatalysts: Advances in theory and experiments, *J. Photochem. Photobiol. C Photochem. Rev.*, 25, 1-29 (2015). https://doi.org/10.1016/j.jphotochemrev.2015.08.003

Fujishima, A., Zhang, X. and Tryk, D. A., TiO_2 photocatalysis and related surface phenomena, *Surf. Sci. Rep.*, 63(12), 515-582 (2008). https://doi.org/10.1016/j.surfrep.2008.10.001

Guo, Q., Zhou, C., Ma, Z. and Yang, X., Fundamentals of TiO_2 photocatalysis: Concepts, mechanisms, and challenges, *Adv. Mater.*, 31(50), 1901997 (2019). https://doi.org/10.1002/adma.201901997

Jose, A., Pai, S. D. K. R., Pinheiro, D. and Kasinathan, K., Visible light photodegradation of organic dyes using electrochemically synthesized MoO_3/ZnO, *Environ. Sci. Pollut. Res.*, 28(37), 52202-52215 (2021). https://doi.org/10.1007/s11356-021-14311-9

Khan, I., Saeed, K., Ali, N., Khan, I., Zhang, B. and Sadiq, M., Heterogeneous photodegradation of industrial dyes: An insight into different mechanisms and rate-affecting parameters, *J. Environ. Chem. Eng.*, 8(5), 104364 (2020). https://doi.org/10.1016/j.jece.2020.104364

Khan, S., Sadiq, M., Kim, D. S., Ullah, M. and Muhammad, N., TiO_2 and its binary $ZnTiO_2$ and ternary $CdZnTiO_2$ nanonanocomposites as efficient photocatalysts for organic-dye degradation, *Appl. Water Sci.*, 12(6), 118 (2022). https://doi.org/10.1007/s13201-022-01628-0

Khlyustova, A., Sirotkin, N., Kusova, T., Kraev, A. and Titov, V., Doped TiO_2: The effect of doping elements on photocatalytic activity, *Mater. Adv.*, 1(5), 1193-1201 (2020). https://doi.org/10.1039/D0MA00171F

Lee, K. M., Lai, C. W., Ngai, K. S. and Juan, J. C., Recent developments of zinc oxide-based photocatalysts in water-treatment technology: A review, *Water Res.*, 88, 428-448 (2016). https://doi.org/10.1016/j.watres.2015.09.045

Mousa, H. M., Alenezi, J. F., Mohamed, I. M. A., Yasin, A. S., Hashem, A. F. M. and Abdal-hay, A., Synthesis of TiO_2@ZnO heterojunction for dye photodegradation and wastewater treatment, *J. Alloys Compds.*, 886, 161169 (2021). https://doi.org/10.1016/j.jallcom.2021.161169

Mousa, S. A., Abdallah, H. and Khairy, S. A., Low-cost photocatalytic membrane modified with green heterojunction TiO_2/ZnO nanoparticles prepared from waste, *Sci. Rep.*, 13(1), 22150 (2023). https://doi.org/10.1038/s41598-023-49516-0

Nur, A. S. M., Sultana, M., Mondal, A., Islam, S., Robel, F. N., Islam, A. and Sumi, M. S. A., A review on the development of elemental and codoped TiO_2 photocatalysts for enhanced dye degradation under UV-vis irradiation, *J. Water Process Eng.*, 47, 102728 (2022). https://doi.org/10.1016/j.jwpe.2022.102728

Ong, C. B., Ng, L. Y. and Mohammad, A. W., A review of ZnO nanoparticles as solar photocatalysts: Synthesis, mechanisms and applications, *Renew. Sustain. Energy Rev.*, 81, 536-551 (2018). https://doi.org/10.1016/j.rser.2017.08.020

Qutub, N., Singh, P., Sabir, S., Sagadevan, S. and Oh, W. C., Enhanced photocatalytic degradation of Acid Blue dye using CdS/TiO_2 nanocomposite, *Sci. Rep.*, 12, 5759 (2022). https://doi.org/10.1038/s41598-022-09479-0

Rana, A., Sonu, S., Sudhaik, A., Kumar, R., Chawla, A., Raizada, P., Chaudhary, V., Ahamad, T., Kaya, S., Kumar, N., Katin, K. P., Hussain, C. M. and Singh, P., Tailoring dual S-scheme based g-C_3N_4/ZnO/TiO_2 ternary photocatalytic system immobilized on floating cork for environmental remediation, *J. Taiwan Inst. Chem. Eng.*, 168, 105914 (2025). https://doi.org/10.1016/j.jtice.2024.105914

Reza, K. M., Kurny, A. S. W. and Gulshan, F., Parameters affecting the photocatalytic degradation of dyes using TiO_2: A review, *Appl. Water Sci.*, 7(4), 1569-1578 (2017). https://doi.org/10.1007/s13201-015-0367-y

Suvathi, S., Rathi, R., Ravichandran, K., Kavitha, P., Ayyanar, M. and Kumar, P. K., Improved

Article in Press

photocatalytic dye degradation and seed germination through enzyme-coupled titanium oxide nanopowder: A cost-effective approach, *Environ. Res*., 218, 114973 (2023). https://doi.org/10.1016/j.envres.2022.114973

Taymaz, B. H., Demir, M., Kamış, H., Orhan, H., Aydoğan, Z. and Akıllı, A., Facile and green synthesis of ZnO nanoparticles for effective photocatalytic degradation of organic dyes and real textile wastewater, *Int. J. Phytoremed.*, 25(10), 1306-1317 (2023). https://doi.org/10.1080/15226514.2022.2150142

Truong, H. T., Truong, H. B. and Nguyen, T. C., ZnO/TiO_2 photocatalytic nanocomposite for dye and bacteria removal in wastewater, *Mater. Res. Exp.*, 11(8), 085003 (2024). https://doi.org/10.1088/2053-1591/ad6bf2

Zhang, Y., Bo, X., Zhu, T., Zhao, W., Cui, Y. and Chang, J., Synthesis of TiO_2-ZnO n-n heterojunction with excellent visible-light-driven photodegradation of tetracycline, *Nanomater.*, 14(22), 1802 (2024). https://doi.org/10.3390/nano14221802

Article in Press